



Research article

Electrical performance enhancement of MHD microgenerators through the longitudinal shaping of the cross-section

F. Trillaud^a, J.E.V. Guzmán^{a,*}, M.A. Ramírez-Trocherie^a, L. Oropeza-Ramos^b

^a Instituto de Ingeniería - UNAM, Coyoacán, 04510, Ciudad de México, Mexico

^b Facultad de Ingeniería - UNAM, Coyoacán, 04510, Ciudad de México, Mexico

ARTICLE INFO

MSC:
0000
1111

Keywords:

MHD
Microgenerator
Shape
Current
Electrolyte
Channel

ABSTRACT

In the present work, the impact that the longitudinal shape of channels has on the current produced in the flow of a magneto-hydrodynamic microgenerator (MHDMG) is studied. The goal is to find the micro-channel geometry via modeling to maximize the current output for low Reynolds and Mach regimes. To carry out this study, a 3D dynamic numerical tool relying on the finite volume method was handled with the open-source software OpenFOAM. It is the base model to study the impact of intricate geometries on the ability to produce energy. An additional steady-state 2D analytical model was also developed to check some basic modeling assumptions. Both models have been experimentally validated on the simplest flow system having a constant square cross-section throughout. The results produced by both models cross-check very well and compare favorably with respect to experimental data. Hence, using the validated numerical tool, three shapes have been further investigated, namely, progressive (linear decrease of the cross-section), arc (parabolic decrease of the cross-section), and wavy (sinusoidal shape). It was found that the arc channel provides the greatest current output for the same volumetric flow. It is therefore the preferred choice for developing high current gain and more efficient MHDMG used in micro-scaled actuators and sensors.

Nomenclature

η	Dynamic viscosity [Pa.s]
$\lambda_{x/y/z,n}$	Eigenvalues along x , y and z coordinates [Rad/m]
\mathbf{B}_a	External magnetic flux density [T]
\mathbf{j}	Current density [A/m^2]
\mathbf{u}	Velocity of the fluid [m/s]
μ_0	Permeability of vacuum [kg.m/s.A]
ν	Kinematic viscosity [m^2/s]
ρ	Mass density of the fluid [kg/m^3]
σ	Electrical conductivity of the fluid [S/m]
A_L	Surface of the conducting wall [m^2]

* Corresponding author.

E-mail address: jguzmanv@ingen.unam.mx (J.E.V. Guzmán).

<https://doi.org/10.1016/j.heliyon.2023.e22305>

Received 28 December 2022; Received in revised form 11 October 2023; Accepted 9 November 2023

Available online 17 November 2023

2405-8440/© 2023 The Author(s). Published by Elsevier Ltd. This is an open access article under the CC BY-NC-ND license (<http://creativecommons.org/licenses/by-nc-nd/4.0/>).

d	Length of one edge of the micro-channel square cross-section [m]
I	Current [A]
L	Length of the micro-channel [m]
p	Pressure [Pa]
S	Cross-sectional area of the constant channel [m ²]
t	Time [s]
u_s	Slip velocity [m/s]
w	Wetted perimeter of the micro-channel [m]
Ha	Hartmann number [-]
N	Stuart number [-]
Re_m	Magnetic Reynolds number [-]
Re	Reynolds number [-]

1. Introduction

In the present work, the currents produced in Magneto-hydrodynamic microgenerators (MHDMG) with specific geometrical configurations are analyzed. Indeed, the effects introduced by the conduit's shape on the currents induced in the fluid have practical relevancy in the development of specialized micro-devices as discussed in [1]. Therefore, understanding how the geometry can impact the current output has a positive outcome when designing more efficient and cheaper MHDMG devices for mass production [2]. It is worth noticing that the subject is scarcely treated in the open literature in the context of energy production at the micro-scale, but widely treated in heat transfer phenomena [3,4].

Research conducted along these lines is further justified, in view of the fact that lab-on-a-chip (LOC) devices, as well as point-of-care devices, designed for health diagnostics, have distinctive design constraints in developing countries. These constraints differ from those designed for similar applications in more developed regions of the World. Among other relevant considerations, the proposed design must consider the absence of ground electricity, the cost of fixed instrumentation, the lack of equipped 'end-use' facilities, and the portability of the device [5,6]. For instance, according to the World Health Organization (WHO), nearly one billion people worldwide receive healthcare attention in facilities with limited access to electricity [7]. In this regard, our miniaturized MHD generator design represents a convenient way to boost the harvested current by occupying a small footprint and substituting mesoscopic batteries. These features allow the development of portable diagnostic platforms to serve regions with underdeveloped medical infrastructure. Another *ad hoc* application of MHDMG is in an autonomous and compact electrophysiology LOC device to characterize the electrical activity of individual neurons. A case of particular interest is based on the current-clamp technique. Overall, miniaturizing certain components in biomedical devices offers a wide range of experimentation possibilities, as described in the Review Neuroscience Goes on a Chip [8].

The elementary principle behind the MHDMG operation involves a conductive fluid that moved through a static background magnetic field, thereby producing an electric current in the bulk of the fluid [9]. Some interesting possibilities may then arise as a result of the steady operation of an MHDMG: a) the current can be harnessed to feed external electronic circuits (e.g. sensors), b) the current may serve to control the flow itself (e.g. slowing the flow through Hartmann breaking), and c) the current may be tailored to facilitate certain interactions in the fluid (e.g. surface treatments). Based on these possibilities, lab-on-a-chip devices can be engineered to exploit the electrophoretic properties of human blood cells [10] in segregation, selection, and drug delivery operations. Already in the micro-pump variant of the MHD process, the capability of fine-tuning the currents instead of the potentials for precise fluid control has demonstrated its virtues in millimetric devices [11]. Modifying the flows and currents through morphological variations of the conduit's cross-section along the channel's length provides additional freedom to the designer. C. Murray et al. (2013) [12] changed the flow by actively controlling the geometry with external potentials acting on electro-active polymer layers. The implication that length-wise peristaltic variations of the micro-channel has on the velocity and Joule heating of biofluids was analyzed in the context of an electrokinetic process [13]. In this case, the motion of the biofluids was found to depend largely on the zeta potentials, as well as the electroosmotic parameter and the applied magnetic field. Combined electromagnetic-hydrodynamic processes were computed theoretically in [14] for rectangular microchannels. An optimal orientation between the channel and the applied fields was noted to favor efficiency. Further modification of the fields and currents at particular locations in the flow system could lead to interesting sensor designs for actuators [15], mixers [16], and wetting devices [17]. Interesting possibilities are also furnished by local variations of the surface charge densities induced by bacteria in biosensors [18]. Since the arrangement of the sensing probes on the functional surface is key to the sensor's operation, one may contend that local manipulation of currents through geometric variations of the MHD process could potentially be exploited to selectively functionalize the sensing surfaces. One attractive advantage of the microgenerator is its apparent lack of bubble formation at the conducting walls.

More in line with the objective of the present paper, M. I. Hasan et al. (2017) numerically explored the effects introduced by cross-sections with different shapes in the pumping action of a microchannel [19]. Simple geometries such as rectangular, circular, and trapezoidal cross-sections were investigated. These sections, however, were constant along the axial direction (i.e. in the direction of the flow). Losses were found to be large in sharply cornered geometries due to secondary flows. As a matter of fact, trapezoidal sections produced the lowest flow rates for the applied conditions. It is clear that the shape of the cross-section is key to modifying the flow properties. In this sense, Parvin et al. recently analyzed the effect of a wavy patterned cavity on the MHD-driven heat transfer process involving an enclosed elliptical cylinder [20]. The authors found that the wavy cavity appears to favor the convective transfer of heat from the heated cylinder to the surrounding nanofluid (water laden with Al₂O₃ nano-particles), particularly at

higher Rayleigh numbers and nano-particle concentrations. Several parameters were modified to establish their respective effect on the thermal process, but the wavy geometry remain constant. The squeezing effect on a micro-cantilever sensor contained in an MHD channel is theoretically explored in [21]. An investigation with a biomedical orientation led C. G. Njingang Ketchate et al. to analyze the hydromagnetic and thermal effects on a fluid model (Casson's fluid) representing blood flowing through a rigid artery with a constant cross-section [22].

Hence, in spite of the number of articles concerned with MHD flows in micro-devices, certain aspects related to the conduit's shape remain to be explored. In particular, the impact of the evolution of the cross-section of the micro-channel in the direction of the flow remains to be deepened. To conduct such a study, a numerical tool was developed in the present work and experimentally validate against a simple case scenario, an MHDMG with a constant squared micro-channel. This simple case is of interest since it can be modeled analytically thereby providing an alternative mean to cross-check the numerical model and additionally giving some insights on the physics of the current generation in a MHDMG. Thus, the analytical solution for the steady-state operation of the squared baseline geometry, as well as the numerical simulations for the full 3D transient analysis, have been cross-checked and compared to experimental data. The Finite-Volume Method (FVM) solver is the free CFD software OpenFOAM V1712 [23,24]. The measurements were obtained from a physical test model of the microgenerator to produce micro-ampère currents into a resistive external electrical circuit. The size of the MHD generator under consideration belongs to the sub-millimeter class. To model the system, a classic MHD approach is employed [25]. Accordingly, some micro-scale effects that include heating, changes in the material properties, or the formation of Helmholtz layers [26] are not considered. However, in view of the fact that the no-slip condition is not satisfied on the polymer walls, the related effect is taken into account in the analytical and numerical model. Most of the existing models have been developed for micro-pumps [27] and can be easily adapted to describe the operation of a microgenerator. The literature reports analytical models for one- and two-dimensional (2D) problems [28,29], while three-dimensional numerical solutions are reported based on Finite Difference Methods (FDM) [30,31], Finite Element Methods (FEM) [32], and Finite Volume Methods (FVM) [33–35]. We chose the FVM as it is the most common approach to dealing with fluids in motion. And for the present work, the basic MHD model provided by OpenFOAM was adapted to process electromagnetic physics.

Having validated the numerical model, a parametric study was then carried out to find the geometry that boosts the generation of current (in a similar way to [19]). For this analysis, the shape of the micro-channel was altered so that the fluid could be naturally accelerated while fixing the magnetic flux density and volumetric flow constant. As the current is related to the velocity, a greater velocity would generate a larger current output. Hence, in addition to the baseline geometry, three shapes have been studied: progressive, arched, and wavy. All three shapes have the same basic square cross-section, the difference resides in the evolution of the shape of the channel over its length, i.e. in the longitudinal (axial) direction of the channel or, in other words, in the direction of the flow. For the progressive channel, the cross-section decreases linearly from the inlet to the outlet. For the arc channel, the longitudinal shape of the channel follows a parabolic curve. The inlet and outlet cross-sections are identical. For the sinusoidal shape, the longitudinal shape of the channel follows a sinusoidal pattern. Here too, the inlet and outlet are identical. It is found that the arc channel yields the largest amount of current for a given flow benefiting from a Venturi effect due to the constriction of the channel. Such simple geometries can increase the energy gain of MHDMG augmenting their efficiency and leading to the manufacture of cheap microsensors and actuators.

2. Description of the microgenerator's operation

The operation of the present microgenerator relies on the motion of an electrolyte, which is forced to flow inside a conduit completely immersed in an externally applied, static, magnetic flux density B_a . The interaction of the charged fluid with the magnetic field induces an electromotive force (or e.m.f.). In turn, the e.m.f. establishes an effective current within the bulk of the fluid [9]. The electrolyte is set in motion by an imposed external pressure gradient. By virtue of the interaction between the induced current and the magnetic flux density, a Lorentz force arises and acts in opposition to the fluid's motion causing, thereby, the so-called Hartmann breaking effect on the flow [36].

The baseline flow system consists of a micro-channel with a constant cross-section (hereafter referred to as the constant channel), a precision piston that supplies a finely tuned volume flow rate, and two permanent (neodymium) magnets that produce a constant magnetic flux across the bulk of the fluid [37]. The electrolyte itself is a saturated solution of sodium chloride (NaCl) diluted in triple-distilled water at a molar concentration of $1.6 \times 10^3 \text{ mol/m}^3$. The constant channel consists of a laser-cut plate made of hydrophobic Polydimethylsiloxane (PDMS). Two transparent pieces of glass, coated with indium-tin-oxide (ITO), constitute the upper and lower walls of the channel. ITO-coated plates ensure an adequate electrical continuity between the fluid and the walls. Moreover, these walls collect the electrical current produced in the fluid and transfer it to an external electrical circuit. Tables 1 and 2 summarize the fluid properties and the relevant characteristics of the micro-channel. Fig. 1 illustrates its basic configuration.

3. Methods

3.1. Baseline analytical model

A simplified model that takes into account the hydrodynamic characteristics introduced by the PDMS walls is considered for the classical Hartmann problem. General assumptions are presented for the baseline model in the low magnetic Reynolds limit (i.e. $Re_m = \sigma \eta u L \ll 1$). In this case, the electrolyte is an incompressible Newtonian fluid that circulates through a channel defined by 4 walls. Mechanical and electrical interactions between the fluid and the solid walls are not modeled. In particular, the electric double

Table 1
Physical properties of the NaCl solution at a molar concentration of $1.6 \times 10^3 \text{ mol/m}^3$ (Note: permeability taken from [1], other properties measured in the laboratory [38]).

Parameter	Symbol	Value	Unit
Electrical conductivity	σ	$12.54^{\pm 0.13}$	S/m
Magnetic permeability	μ_0	$4\pi \times 10^{-7}$	$\text{kg}\cdot\text{m}/\text{s}^2\cdot\text{A}^2$
Mass density	ρ	$1050^{\pm 12.6}$	kg/m^3
Dynamic viscosity	η	$2.3^{\pm 0.035} \times 10^{-3}$	Pa.s
Kinematic viscosity	ν	2.19×10^{-6}	m^2/s

Table 2
Geometric dimensions of the channel (see Fig. 2).

Parameter	Symbol	Value	Unit
Channel length	L	$24^{\pm 0.5} \times 10^{-3}$	m
Edge length	d	$1.2^{\pm 0.5} \times 10^{-3}$	m
Wetted perimeter	$w = 4d$	4.8×10^{-3}	m
Cross-sectional area	$S = d^2$	1.44×10^{-6}	m^2

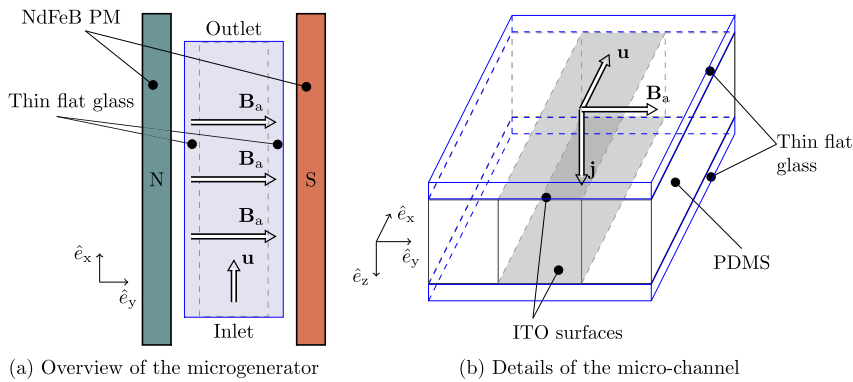


Fig. 1. Microgenerator with a square cross-sectional channel and two permanent magnets. To generate current, an electrolyte is forced to flow into the channel at the velocity \mathbf{u} under a constant applied magnetic flux density \mathbf{B}_a . (a) shows a side view of the microgenerator. (b) shows a top view with details of the channel (2 thin flat pieces of glass coated with ITO and 2 PDMS walls).

layers are ignored in this approximation, since the electric potential measured in the actual experimental device is of the order of 10^{-5} V [38], which is inversely proportional to the time-scale for electric screening [39]. On the other hand, the magnetic flux density is constant and homogeneous in the entire flow field. Even though surface tension effects are present at the measuring port, they imply a nearly constant-pressure offset in the steady-state regime.

Hydro-electrical interactions in the fluid are accounted for by the Lorentz force term introduced in the Navier-Stokes equations. In view of these considerations, the balance equations for the conservation of mass and linear momentum read (e.g. [9,40])

$$\nabla \cdot \mathbf{u} = 0, \tag{1}$$

$$\frac{D\mathbf{u}}{Dt} = -\frac{1}{\rho} \nabla p + \nu \nabla^2 \mathbf{u} + \frac{1}{\rho} \mathbf{j} \times \mathbf{B}_a \tag{2}$$

The fluid's mass density, ρ , and kinematic viscosity, $\nu = \eta/\rho$, are constant properties, while \mathbf{u} and p represent the local values of the velocity and pressure fields, respectively. The Lorentz force per unit volume is determined by the current density \mathbf{j} [A/m²] (induced in the fluid by virtue of its motion) and the applied magnetic flux density, $\mathbf{B}_a = B_a \hat{\mathbf{e}}_y$, such that

$$\mathbf{j} = \sigma (\mathbf{u} \times \mathbf{B}_a) \tag{3}$$

where σ is the electrical conductivity of the electrolyte.

Conservation of the electrical charge in the steady-state regime implies $\nabla \cdot \mathbf{j} = 0$ and, consequently, the total current I [A] generated by the microgenerator is given by

$$I = \int_{A_L} \mathbf{j} \cdot d\mathbf{a} \tag{4}$$

Note that $A_L = Ld$ [m²] represents the area of the conducting wall taken along the channel's length L [m], as illustrated in Fig. 2.

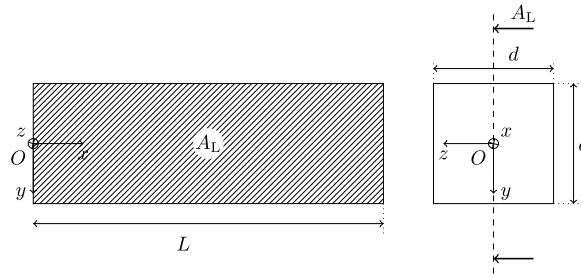


Fig. 2. Baseline geometry. The micro-channel of length L has a constant square cross-section ($d \times d$). This geometry was chosen for its simplicity to model analytically and to implement experimentally.

The analytical solution is obtained in Cartesian coordinates for the steady-state operation of a constant cross-section device. These conditions are satisfied by making $D\mathbf{u}/Dt = \partial\mathbf{u}/\partial t + \mathbf{u} \cdot \nabla\mathbf{u} = 0$ in eq. (2). Two cases are subsequently considered: a) a flow that satisfies the no-slip condition ($u_x = 0$) on all four walls of the channel, and b) a flow that satisfies a finite slip-velocity condition ($u_x = u_s$) on all four walls. The latter is expected to be sufficiently adequate for the case study at hand because two of the channel's walls are made of a hydrophobic dense polymer (PDMS). Consequently, the normal velocity components vanish on the impermeable walls, and $u_y(\pm d/2, z) = u_z(y, \pm d/2) = 0$ [m/s]. Therefore, the fully developed flow is completely defined by the two-dimensional velocity field $\mathbf{u} = u_x(y, z)\hat{\mathbf{e}}_x$. Under similar considerations to those discussed by G. Ibañez et al. [40], equation (2) may be developed into

$$\frac{\partial^2 u_x}{\partial^2 y} + \frac{\partial^2 u_x}{\partial^2 z} - \frac{\text{Ha}^2}{L^2} u_x = \frac{1}{\eta} \frac{dp}{dx} \tag{5}$$

where the quantity $\text{Ha} = B_a L \sqrt{\sigma/\eta}$ defines the Hartmann number (a measure of the ratio between Lorentz and viscous forces); η represents the dynamic viscosity, σ the electrical conductivity, B_a the magnetic flux density, and L the length of the channel. On average, the pressure gradient is constant and can thus be expressed as $dp/dx \approx \Delta p/L$, with $\Delta p = p_{\text{in}} - p_{\text{out}}$ accounting for the total pressure drop across the channel. Although diffusion effects dominate over advection effects of the magnetic flux density (since $\text{Re}_m \sim 10^{-10}$) the flow is assumed to remain in thermal equilibrium with the environment in this relatively slow incompressible flow regime. Furthermore, the smallness of Re_m also implies that the induced field is extremely weak with respect to the externally applied field, and so its effects may be ignored [9]. Such approximations greatly simplify the model because the electric field can also be conveniently decoupled from the magnetic field [40].

In view of the preceding arguments, equation (5) is integrated with the method of separation of variables (e.g. [41]). The separation procedure is straightforward in Cartesian coordinates and yields the solution

$$u_x(y, z) = u_s + \sum_{n=1}^{+\infty} a_n \left[1 - \frac{\cosh(\lambda_{z,n} z)}{\cosh(\lambda_{z,n} d/2)} \right] \cos(\lambda_{y,n} y) \tag{6}$$

whose coefficients

$$a_n = (-1)^n \left(\frac{4}{\pi \eta \lambda_{z,n}^2 (2n-1)} \right) \left(\frac{\Delta p}{L} + \frac{\text{Ha}^2}{L^2} \eta u_s \right), \quad n \in \mathbb{N} \tag{7}$$

are determined by applying the boundary conditions defined in this case. The eigenvalues along the y - and z -directions are accordingly given by

$$\lambda_{z,n} = \sqrt{\text{Ha}^2/L^2 + \lambda_{y,n}^2} \tag{8}$$

and

$$\lambda_{y,n} = (2n-1)\pi/d \tag{9}$$

Clearly, the slip-velocity term in eq. (6) becomes $u_s = 0$ for no-slip condition and $u_s \neq 0$ for finite-slip condition. An accurate estimate of the finite-slip velocity can be obtained from the actual experimental data (refined solutions explicitly derived in terms of the slip lengths can be found in [42]). Based on the flow rates and the pressure drop measured in the laboratory (see section 3.3), the average velocity is computed as $\bar{u} = q/S$ and then compared with the value given by eq. (6). Knowing the expression of the average velocity \bar{u} over the cross-section of the channel from eq. (6) and its relation with the volumetric flow rate, it is possible to infer the slip velocity whose expression is given below

$$u_s = \frac{q - \frac{\Delta p}{L} \sum_{n=1}^{+\infty} c_n \left[d - \frac{2}{\lambda_{z,n}} \tanh\left(\lambda_{z,n} \frac{d}{2}\right) \right]}{d^2 + \frac{\text{Ha}^2 \eta}{L^2} \sum_{n=1}^{+\infty} c_n \left[d - \frac{2}{\lambda_{z,n}} \tanh\left(\lambda_{z,n} \frac{d}{2}\right) \right]}, \tag{10}$$

with coefficients

$$c_n = -\frac{8}{\pi\eta\lambda_{z,n}^2\lambda_{y,n}(2n-1)}, \quad n \in \mathbb{N} \tag{11}$$

This expression gives the relation of the slip velocity with the characteristics of the channel and the properties of the fluid. This expression can be then used in the numerical model if required to get the proper boundary conditions. Here, the estimated values indicate that this velocity represents only 2% to 5% of the average velocity, \bar{u} , for the volume flow-rates of interest, q , which vary in the interval from 10 μ L/s to 40 μ L/s. Consequently, the slip velocity was disregarded to simplify the subsequent analysis. The impact of this choice was further assessed by estimating the induced currents for different slip velocities. It was found that the finite slip velocity had, indeed, a negligible effect on the pressure and the induced currents. Overall, the relative change was less than 4% for the pressure and 2% for the current (at $B_a = 0.3$ T for the prescribed volume flow rates). These values are well within the experimental errors (see section 3.3 for details).

Theoretical estimates of the volume flow rates for the cases of interest can be obtained through direct integration by using the expression for the velocity

$$q = \int_A \mathbf{u} \cdot \mathbf{d}\mathbf{a} = d^2u_s + d^2 \sum_{n=1}^{+\infty} b_n \left[1 - \frac{2}{\lambda_{z,n}d} \tanh\left(\lambda_{z,n}\frac{d}{2}\right) \right] \tag{12}$$

where A represents the channel's cross-section. The expansion coefficients are

$$b_n = -\frac{8}{\pi\eta\lambda_{z,n}^2\lambda_{y,n}(2n-1)} \left(\frac{\Delta p}{L} + \frac{\text{Ha}^2}{L^2} \eta u_s \right), \quad n \in \mathbb{N} \tag{13}$$

In turn, the current generated in the channel is computed from (3)

$$I = \sigma B_a \int_{A_L} u_x \, da = \sigma B_a L d \left[u_s + \sum_{n=1}^{+\infty} b_n \left(1 - \frac{1}{\cosh(\lambda_{z,n}d/2)} \right) \right] \tag{14}$$

Equations (6), (12) and (14) were solved with an in-house code (programmed in Python 3.6) in which up to 50 terms of the series were considered.

3.2. Numerical model

New geometrical configurations of the channel were investigated by performing numerical simulations with the MHD solver contained in the open-source software OpenFOAM [43]. In this solver, the divergence-free magnetic flux density was ensured by means of the same approach as of the Pressure-Implicit with Splitting of Operators (or PISO) algorithm that is used to compute the pressure-velocity coupling in the Navier-Stokes equation (2) [44]. The derived algorithm is referred to as B-PISO, B for the magnetic flux density [45]. It should be noted that the PISO algorithm is a well-established numerical scheme. It is part of the classic algorithms to treat incompressible flows alongside the SIMPLE algorithm. It was proposed in the 1980s demonstrating robustness and stability at a fast computational time compared to the latter [46]. By introducing a fictitious magnetic-pressure gradient, $-\nabla(p_m)$, on the left-hand side of eq. (3), the PISO algorithm could be adapted to tackle MHD problems. The details of the implementation of the algorithm can be found in the manual of the MHD solver (mhdFoam) of the OpenFOAM [47].

The magnetic pressure together with the Maxwell-Faraday equation, $\nabla \times \mathbf{j} = -\sigma \partial \mathbf{B} / \partial t$, this yields the following set of (coupled) equations [48]

$$\nabla \cdot \mathbf{u} = 0 \tag{15}$$

$$\frac{\partial \mathbf{u}}{\partial t} + (\mathbf{u} \cdot \nabla) \mathbf{u} - \nu \nabla^2 \mathbf{u} - 2\gamma_m (\mathbf{B}_a \cdot \nabla) \mathbf{B}_a + \gamma_m \nabla^2 |\mathbf{B}_a|^2 = -\frac{1}{\rho} \nabla(p) \tag{16}$$

$$\frac{\partial \mathbf{B}_a}{\partial t} - \alpha_m \nabla^2 \mathbf{B}_a + \nabla \cdot (\mathbf{u} \mathbf{B}_a) - (\mathbf{B}_a \cdot \nabla) \mathbf{u} = -\nabla(p_m) \tag{17}$$

in which

$$\mathbf{j} \times \mathbf{B}_a = \frac{1}{\mu_0} (\mathbf{B}_a \cdot \nabla) \mathbf{B}_a - \frac{1}{2\mu_0} \nabla^2 |\mathbf{B}_a|^2 \tag{18}$$

and

$$\nabla \times (\mathbf{u} \times \mathbf{B}_a) = (\mathbf{B}_a \cdot \nabla) \mathbf{u} - \nabla \cdot (\mathbf{u} \mathbf{B}_a) \tag{19}$$

were used. Also, note that $\gamma_m = 1/(2\rho\mu_0)$ and $\alpha_m = 1/(\sigma\mu_0)$.

The spatial discretization of equations (15), (16) and (17) was realized within the framework of the Finite Volume Method, and the time integration was handled with an Implicit Euler Method. Stability and convergence were ensured since the Courant-

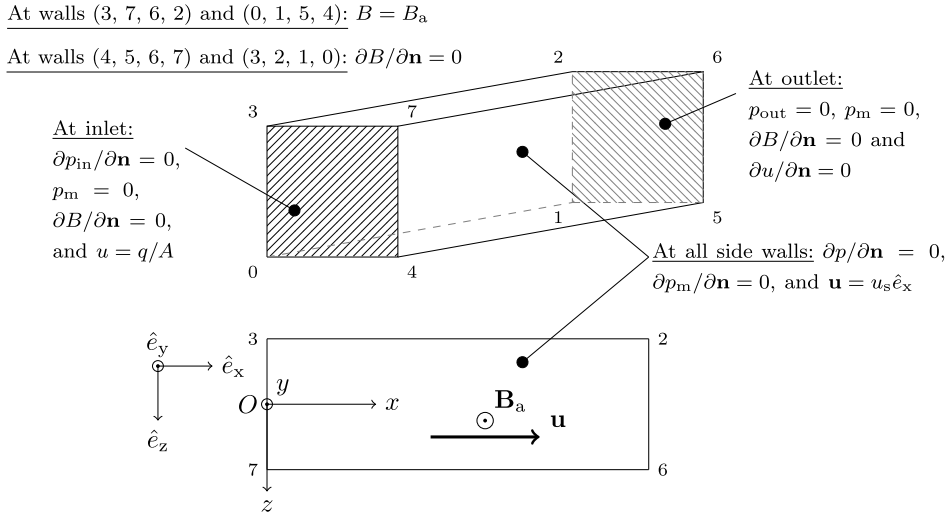


Fig. 3. Boundary conditions of the baseline geometry for the numerical model. These boundary conditions are the same for the other geometries studied here.

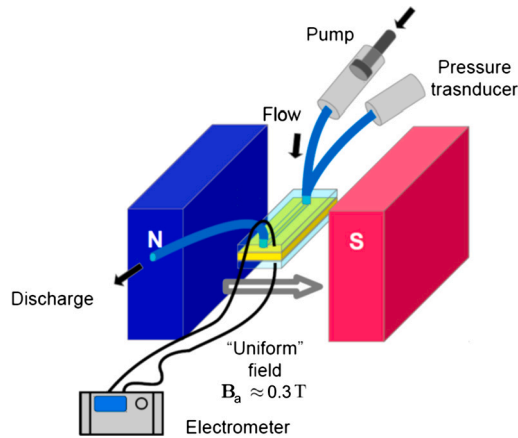


Fig. 4. Schematic drawing of the apparatus used in the experimental setup. The micro-channel is found between the two permanent magnets.

Friedrichs-Lewy number was below 0.4 for the smallest time-step ($\Delta t \approx 5$ ms). The overall simulation time was set to 2 s, well within the steady-state regime. Finally, Fig. 3 illustrates the boundary conditions under consideration for the baseline model and other geometries.

3.3. Experiments

Experiments were carried out to validate the predictions of the analytical and the numerical baseline models. Fig. 4 shows a diagram of the experimental setup. A Keysight B2987A Electrometer (with a minimum current resolution of 10^{-17} A) was connected to the electrically conducting walls of the channel, thereby effectively closing the electrical circuit.

A Honeywell High Accuracy Silicon Ceramic Differential Pressure Sensor (model HSCDRR001NDA-A5) was installed to measure the pressure drop across the channel. In addition, a high-accuracy KD-Scientific picoliter pump (model Legato 185) was connected to the inlet. A finely tuned volume-flow rate of electrolyte was supplied within the interval ranging from 10 to $40 \mu\text{L/s}$ (i.e. 1.0 to $4.0 \times 10^{-8} \text{ m}^3$). A Hall effect probe was placed on top of the channel to measure the magnetic flux density; on average, the registered value was 0.3 ± 0.3 T. A Brookfield DV2T viscometer was used to verify the actual viscosity value in each test.

The electrolyte was created by saturating triple-distilled water with sodium chloride to a concentration that maximized its electrical conductivity. Its electrical conductivity was subsequently determined with an Oakton PC2700 series instrument (with a resolution of 0.01/0.1 Ω and accuracy of 1% across the full scale). Relevant physical properties of the electrolyte are summarized in Table 1. Further details on the laboratory procedures may be consulted in [38].

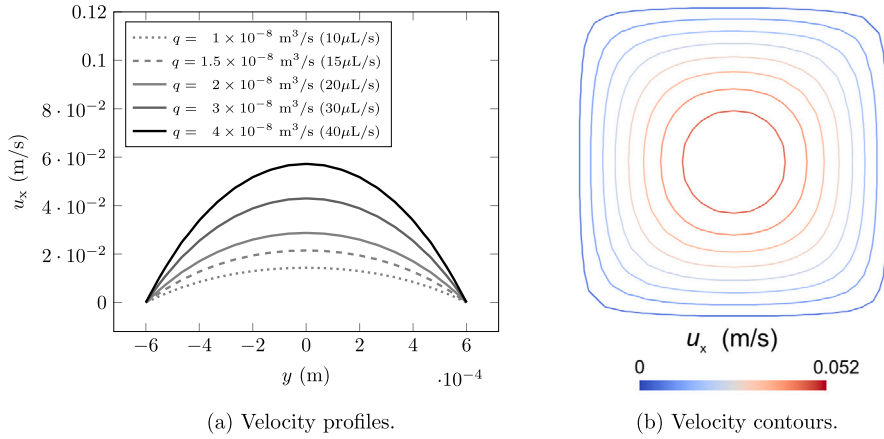


Fig. 5. Numerical results of the velocity profiles for $B_a = 0.3$ T. (a) Computed velocity profiles over a line crossing the cross-section of the channel in the Oy direction at mid-length into the channel. (b) Contours of the velocity over the cross -section of the channel at the same position for $q = 40 \mu$ L/s (4×10^{-8} m³/s).

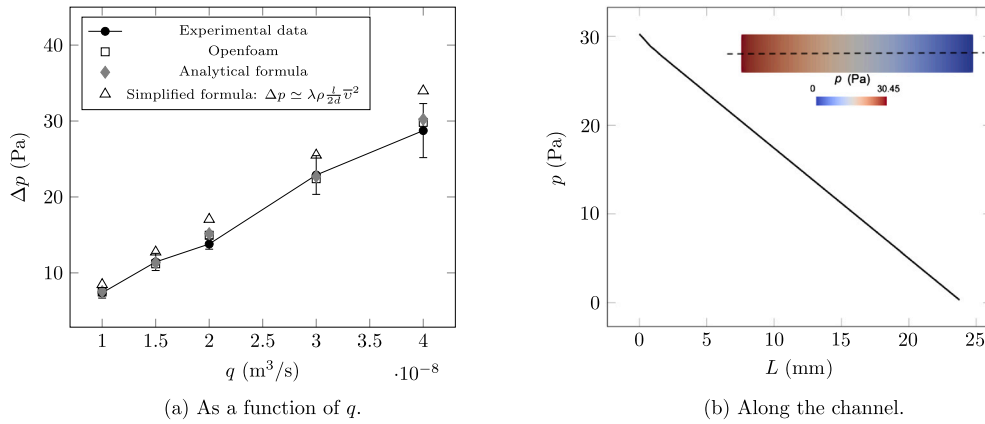


Fig. 6. Numerical and experimental results of the pressure for $B_a = 0.3$ T. (a) Measured and computed relative pressures over the channel ($\Delta p = P_{in} - P_{out}$). (b) Simulated pressure p along the length of the channel for $q = 40 \mu$ L/s. The dashed line in the inserted figure represents the line over which the pressure is plotted. The inserted figure shows the map of the pressure over the surface A_L .

4. Results

The total pressure drop Δp and the current I predicted by the analytical and numerical models were contrasted with the experimental measurements obtained for the previously stated volume flow rates. In addition, the velocities predicted by both types of models were also compared. Fig. 5a shows the (numerically) computed velocity profile at a cross-section located midway between the inlet and outlet of the channel. The velocity contours shown in Fig. 5b are in full agreement with those produced by the analytical solution. No Hartmann breaking effects are discernible in these profiles [49]. This was anticipated in view of the fact that the Hartmann number is quite low, i.e. $Ha \approx 4.4 \times 10^{-2}$ (see Table 3).

In accordance with previously reported investigations, the values of all relevant dimensionless parameters are consistent with the experimental ranges for this kind of device [1]. Besides the Hartmann number, the Magnetic Reynolds and the Stuart numbers also indicate that the electromagnetic forces are negligible with respect to the viscous and inertial forces. Therefore, the motion of the fluid is essentially governed by viscous and inertial forces rather than electromagnetic forces. This explains why the Hartmann-breaking effect is hardly noticeable in the present case.

To check the consistency of the results, three different ways of calculating the pressure over the length of the channel ($\Delta p = P_{in} - P_{out}$) are compared to the experimental measurements so that Fig. 6a shows: 1) the experimentally measured pressure Δp_{ex} , 2) the pressure computed with the (OpenFOAM) numerical model, 3) the pressure obtained with the analytical formula and 4) the pressure calculated with a simplified analytical model that assumes laminar flow with a friction coefficient given by $\lambda = 64/Re$, but without the Hartmann effect. A good agreement is observed between the models and the experimental measurements. Similarly, Fig. 6b shows the position-dependent development of the pressure, $p(x)$, along the channel for $q = 40 \mu$ L/s. Except for the slight entrance effect caused by the development of the flow at the inlet of the channel, the remaining part of the pressure profile is quasi-linear. The respective entrance length is $l_e < 2$ mm, that is $l_e/L \approx 0.08$.

Table 3
Relevant magnetic and fluid numbers for $B_a = 0.3$ T and $q = 40 \mu$ L/s [1].

Parameter	Expression	Value	Comment
Reynolds number	$Re = \frac{uL}{\nu}$	15.1	Laminar flow
Magnetic Reynolds number	$Re_m = \mu\sigma uL$	1.3×10^{-10}	magnetic diffusivity \gg advection
Hartmann number	$Ha = B_a L \sqrt{\frac{\sigma}{\eta}}$	4.4×10^{-2}	Lorentz force \ll viscous force
Stuart number	$N = \frac{L\sigma B_a^2}{\rho u}$	5.1×10^{-4}	Lorentz force \ll inertial force

The currents produced with an external field $B_a = 0.3$ T are compared in Fig. 7a. The plots correspond to the computed currents as well as the experimental measurements for different flow rates. Error bars are provided for both the experimental data and the analytical predictions. In the former case, the deviations from the mean behavior were determined via the statistical treatment of the data, with the mean and the (unbiased) standard deviation estimates respectively given by $I = 1/N \sum_{n=1}^N I_n$ and $\sigma_I = \sqrt{1/(N-1) \sum_{n=1}^N (I_n - I)^2}$ (e.g. [50]). For the latter case, however, a Monte Carlo process was implemented to compute the average value and the standard deviation of the results fed into the model; the input parameters were assumed to follow normal distributions. The corresponding average and standard deviation values of the input parameters are collected in Tables 1 and 2. Both models provide similar results in the micro-ampere interval from 1.5 to 4 μ A. Nevertheless, the predicted values diverge from the experimental measurements for volume flow rates above 20 μ L/s. While the computed current I evolves linearly with q (as expected, since $I = \tilde{u}_x B_a A$ on average), the experimental current appears to flatten with increasing flow rates.

Various factors may lead to variations in the measured currents. Presently, the possible, albeit less studied, effects introduced by wall deformations of the channel are quantified. It is recalled that the channel is made of a flexible plastic material susceptible to mechanical deformation. It should be noted that the assumptions of our basic modeling approach do not account for chemical interactions between the electrolyte and the walls, the polarization of the fluid (capacitor effect), and coupling effects with the external electrical circuit. Furthermore, the static deformation of the walls is considered to be small because the electric potential is low ($\sim 10^{-5}$ V) and the related force is $F \propto V^2$ (where V is the voltage) [51]. Instead, we focus on the analysis of the two cases illustrated in Fig. 8: 1) the narrowing of the channel’s cross-section caused by slight material dilatation and contraction effects in the low flow rate regime, and 2) a channel’s cross-section expansion caused by the mechanical action of the pressures produced with sufficiently high flow rates. The percentages shown in the figure indicate the degree of deformation measured at the channel’s midsection.

The simulations indicate that the deformation of the walls can play a major role in the current output. This can be observed in the plots of Fig. 7b, where the improved agreement between results is notable. Note that the lowest deformation corresponds to a 25% reduction of the mid-section at $q = 10 \mu$ L/s, while the highest deformation corresponds to a 75% expansion at $q = 40 \mu$ L/s. The obtained results suggest that (soft) PDMS walls may undergo significant deformations during the operation of the microgenerator at high volume flow rates. Nevertheless, other previously mentioned effects must be subjected to further investigations [26]. Indeed, it is expected that a non-negligible part of the discrepancy in the current may be not solely due to the mechanical deformation providing a clearer picture of the saturation of the current at increasing flow. Hence, in a future continuation of the present work, the mechanical and electrical (capacitive) effects impacting the magnitude of the generated current will be explored by changing the properties of the material and the fluid (e.g. by replacing the electrolyte with a liquid metal to determine the extent to which ionic charges affect the nature of the process) alongside a numerical model including more refinements such as the electrostatic field developed between the conductive walls of the channel.

4.1. Impact of the channel’s geometry on the generated current

In view of the impact that the variations of the cross-section have on the generated current, it is relevant to study the effects produced by specific shapes of the channel. Three distinct geometries which may boost the current output for the same volume flow rate of the baseline model were tested. Thus, in addition to the constant channel (a), the progressive channel (b), the arched channel (c), and the wavy channel (d) illustrated in Fig. 9 are analyzed. The progressive channel is characterized by a constant decrease of the cross-section in the Oz direction (i.e. along the length of the channel). The arched channel resembles a de Laval nozzle with a symmetrical contraction-expansion design about the throat section. The wavy channel has a sinusoidal development of all its walls in the Oz direction. Note that the Oz direction was chosen to maintain the surface area over which the current is computed, A_L , equal in every case.

Fig. 10 shows the currents produced by each geometry. For cases (a) and (c), the velocity profile in the longitudinal mid-plane (shown as a colored map) is not fully symmetrical with respect to the center of the channel. This slight asymmetry is due to the non-linear development of the pressure near the inlet 6b. The entrance effect is amplified by the geometry and terminates in the fully developed flow region.

In comparison with the baseline case (a), the best option to boost the current output is the arched channel (c). On the other hand, the progressive channel (b) leads to a substantial decrease in the current. For a constant surface A_L and a constant applied magnetic flux density B_a , the current depends essentially on the local velocity u_x , as indicated by (14). Clearly, the maximum acceleration of

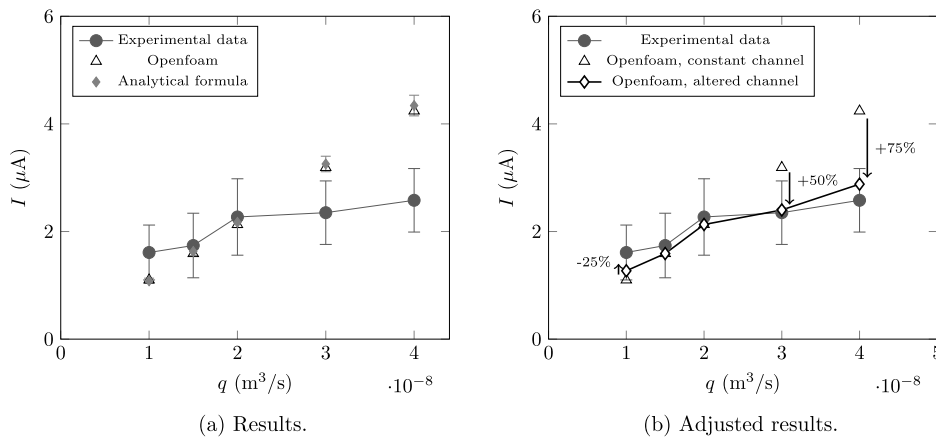


Fig. 7. Measured and computed currents at $B_a \approx 0.3$ T. (a) experimental data compared to results obtained from the OpenFOAM software and the analytical formula. (b) adjustment of the numerical results by deforming the shape of the channel.

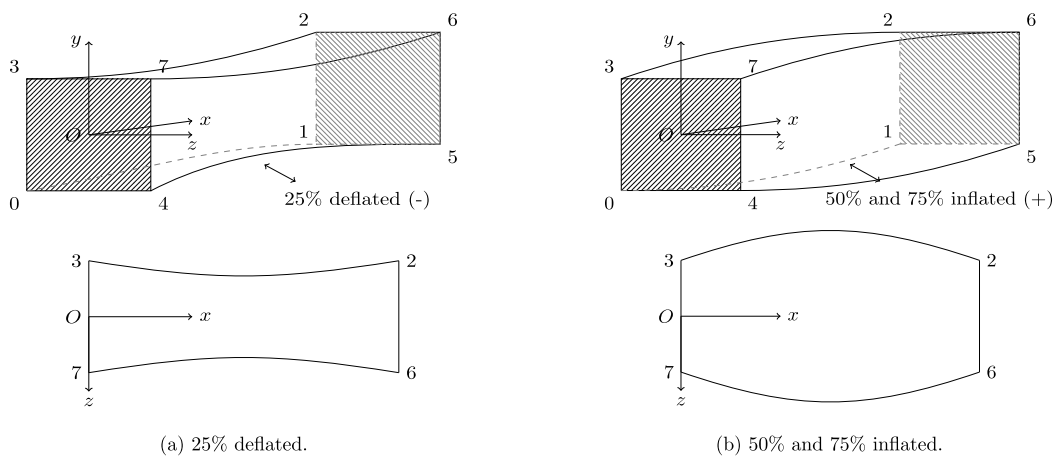


Fig. 8. (a) deflated channel by -25% at mid section over Oy and Oz direction. (b) inflated channel by +50% and +75% at mid section over Oy and Oz direction.

Table 4

Average velocities $\bar{u}_x = \Sigma u_{x,n}/N$ across the plane (Oxy) for $B_a = 0.3$ T and $q = 40 \mu L/s$. The relative value is referred to the case (a). “-” and “+” indicate loss and gain, respectively.

Case study	Value [cm/s]	Relative value = $\left(\frac{\bar{u}_x - \bar{u}_{x,ref}}{\bar{u}_{x,ref}} \right) [\%]$
Constant channel (a)	3.89	Reference, $\bar{u}_{x,ref}$
Progressive channel (b)	3.10	-20
Arc channel (c)	6.25	+61
Wavy channel (d)	1.14	-71

the fluid is attained at the throat of the arched channel in view of the Venturi effect (see Fig. 11c). In the case of the progressive channel (Fig. 11b) the average velocity is significantly lower than the one produced by all other geometries for the same volume flow rate (e.g. 1.85 cm/s against 2.77 cm/s for the constant channel). Note that the acceleration towards the outlet is not enough to compensate for the reduced average velocity. With the wavy channel (d) the Venturi effect emerges at the contracted sections which are periodically located along the channel (Fig. 11d). Even though the current produced by this geometry is not as high as in the case of the arched channel, the fact that the electric field can be enhanced in certain controllable parts of the flow system offers interesting possibilities for potential applications in micro-devices [19].

Table 4 summarizes the average velocities in each case for the prescribed applied magnetic field and flow rate ($B_a = 0.3$ T and $q = 40 \mu L/s$). It is noteworthy that the maximum velocity gain of +61% is attained with the arched channel (c), while the largest percent velocity reduction of -71% is attained with the progressive channel (d). Clearly, the current’s gain and loss are proportional to these velocities’ gain and losses.

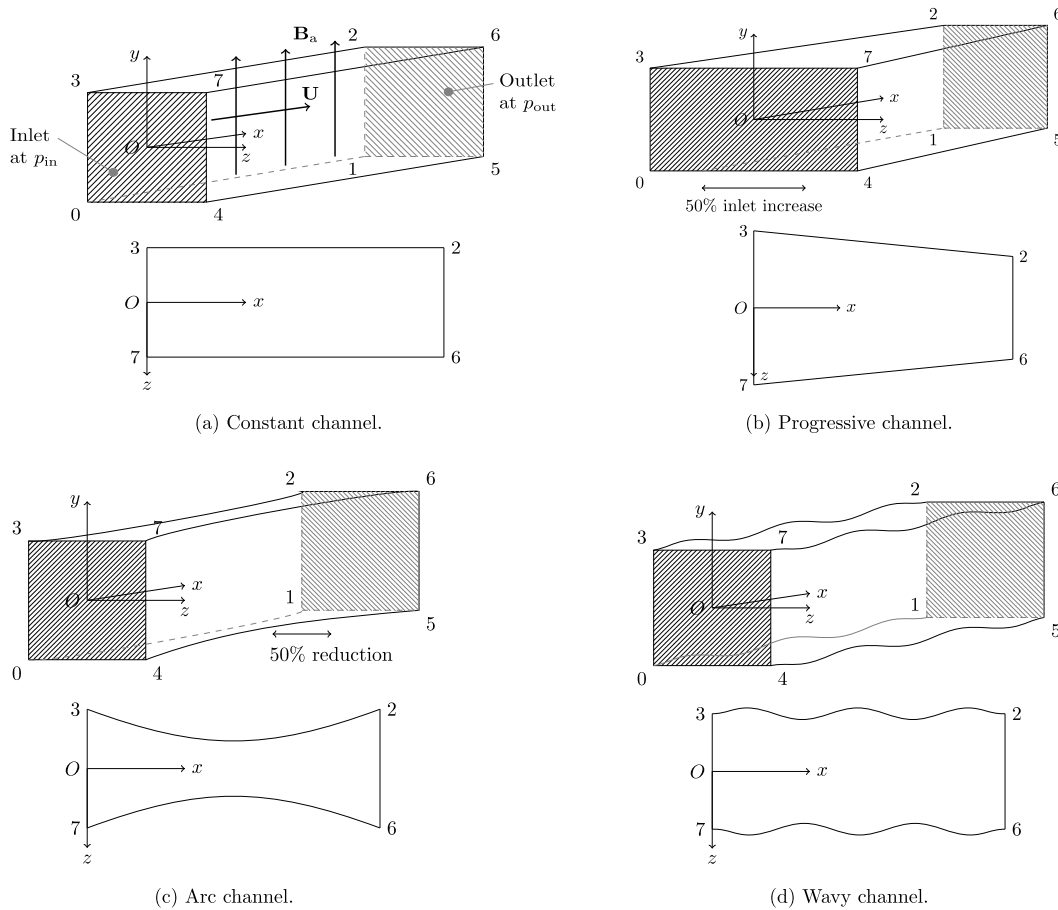


Fig. 9. Geometries of interest: (a) constant channel (baseline case), (b) progressive channel, (c) arc channel, and (d) wavy channel. The wavy shapes lie in the (3, 7, 6, 2) and (0, 1, 5, 4) planes with a wave amplitude representing 50% of the channel edge d .

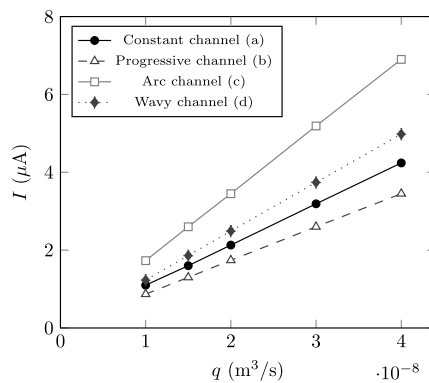


Fig. 10. Comparison of currents obtained for the three geometries investigated ($B_a = 0.3$ T).

5. Discussion

A microgenerator was built to determine the main parameters affecting the current output to an external circuit. The flow system involved a square cross-section channel made with two PDMS (soft) walls and two (electrically conducting) ITO walls. This microgenerator was fully embedded in the homogeneous region of an externally applied magnetic induction field generated by neodymium magnets.

Analytical and numerical models (developed in OpenFOAM) were validated with the experimental data collected under controlled conditions in the laboratory. A channel with a constant cross-section served as a baseline case. The currents measured in this baseline

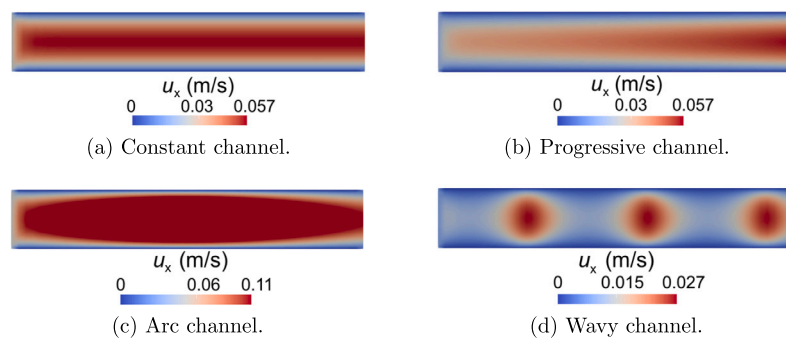


Fig. 11. Velocity magnitude in the plane (Oxy). The images were re-scaled in the Ox direction by a factor of 0.3 to fit into the frame of the figure.

experimental model were found to be slightly above 2.5×10^{-6} A for volume-flow rates of 4.0×10^{-8} m³/s ($q = 40 \mu$ L/s) and magnetic field of $B_a = 0.3$ T.

The observed discrepancies between the currents predicted by the model and the experimental data require further investigation. The pressure-driven expansion of the PDMS walls could account for the decrease of the current with significant deformations of the channel but it is certainly not the only factor here. The complex effects related to the motions of ionic charges in the bulk of the fluid could have a strong effect on the current output as well. Future works should involve a refined model that includes factors, such as the capacitance effect via the generation of an electrostatic field between the conductive walls of the channel. Experiments combined with modeling should provide the means to pinpoint the origin of the nonlinear dependence of the current on the volume flow rate.

Beyond the naturally occurring mechanical deformation, it was shown that the shape of the channel can be used to control the current generation. In particular, it is possible to boost, or decrease, the current output by means of simple geometrical variations of the cross-section. Maximum current output was achieved with an arched channel, whereas the progressive channel lead to a current reduction. It appears that Venturi-shaped channels would be the best option to produce significant current gains. On the other hand, wavy channels produce an increased current output in specific places inside the flow system. In this sense, one could profit from such manipulations of the electric field and the associated electrical current in specific applications by sectioning the electrodes of the channel thereby providing different currents arising from different local geometries, for instance. Clearly, the geometrical variations of the cross-section represent a simple and practical way to control the internal electric field and power output of the microgenerator in applications. Interestingly, the behavior found here can be also applied to the most common micro-pumps as they rely on the same physics.

6. Conclusion

The present work dealt with the impact of the longitudinal/axial geometry of the channel on the current output of a micro-generator for low Reynolds and Mach regimes in the sub-millimetric scale. A numerical model based on the finite volume method was solved with the open-source software OpenFOAM and validated to study different geometries and find the best one to maximize the current gain of the device. Experimental data were obtained from a microgenerator made of a constant squared-shaped cross-sectional micro-channel. A 2-D analytical solution for the steady state was obtained to gain further insight into the underlying physics, as well as to provide some checks on the fundamental assumptions of the numerical model.

It was observed that the models agree reasonably well with experimental data if one accounts for the mechanical deformation of the micro-channel under the pressure of the fluid. Having validated the numerical model, different shapes have been studied, progressive (the cross-section decreases linearly over the length of the channel), arc (parabolic shape), and wavy (sinusoidal pattern). We found that the arched channel supplies the largest amount of current for a given flow benefiting from the Venturi effect provided by the natural concave shape of the channel. This is, therefore, the preferred geometry, as it is simple enough for easy manufacturing while maximizing the current gain and, consequently, the overall efficiency.

Future spin-off works can encompass experimental and numerical tasks. The numerical model can be further improved by adding the electrical potential and by providing the basis for the capacitor effect found in the microgenerator. Different fluids and geometries can be studied experimentally providing further data to find the best combination between material properties and geometries.

Ethics declarations

Review and approval by an ethics committee was not needed for this study because no living organisms or ecosystems were harmed with the experiments.

CRediT authorship contribution statement

F. Trillaud: Formal analysis, Software, Writing – original draft. **J.E.V. Guzmán:** Conceptualization, Formal analysis, Writing – original draft, Writing – review & editing. **M.A. Ramírez-Trocherie:** Formal analysis, Validation. **L. Oropeza-Ramos:** Data curation, Resources, Writing – review & editing.

Declaration of competing interest

The authors F. Trillaud, J.E.V. Guzmán, M. Ramírez-Trocherie, and L. Oropeza declare that they have no conflict of interest concerning the development of the work, nor with the information (data, methods, results, etc.) contained in the paper.

Data availability

The data will be made available on request.

Acknowledgements

This research was financially supported by Instituto de Ingeniería UNAM through grant No. 5342, IING/SA/037/2015. The authors wish to thank Prof. Luis Fernando Olguín Contreras from UNAM's School of Chemistry for facilitating the experimental characterization of the electrolyte. We also thank Jimmy Rojas, a participant in the MIT-Mexico exchange program, for his early help in the implementation of the OpenFOAM model. M. Ramírez-Trocherie wishes to thank Instituto de Ingeniería UNAM (Grant No. 5342, IING/SA/037/2015) for sponsoring the development of his Master's thesis.

References

- [1] N.-T. Nguyen, Micro-magnetofluidics: interactions between magnetism and fluid flow on the microscale, *Microfluid. Nanofluid.* 12 (2012) 1–16, <https://doi-org.pbidi.unam.mx:2443/10.1007/s10404-011-0903-5>.
- [2] S.K. Tiwari, S. Bhat, K.K. Mahato, Design and fabrication of low-cost microfluidic channel for biomedical application, *Sci. Rep.* 10 (2020) 9215, <https://doi.org/10.1038/s41598-020-65995-x>.
- [3] Z. Rehman, F. Ahmad, H.A. Muhammad, F. Riaz, H.M.U. Ayub, M. Hasan, M. Lee, Study of thermal characteristics of energy efficient micro channel heat sinks in advanced geometry structures and configurations: a review, *Front. Energy Res.* 10 (2022) 951066, <https://doi.org/10.3389/fenrg.2022.951066> (12pp).
- [4] B. Kundu, S. Saha, Review and analysis of electro-magnetohydrodynamic flow and heat transport in microchannels, *Energies* 15 (19) (2022) 7017, <https://doi.org/10.3390/en15197017> (51pp).
- [5] C.D. Chin, V. Linder, S.K. Sia, Lab-on-a-chip for global health: past studies and future opportunities, *R. Soc. Chem.* 7 (2007) 41–57, <https://doi-org.pbidi.unam.mx:2443/10.1039/B611455E>.
- [6] P. Yager, G.J. Domingo, J. Gerdes, Point-of-care diagnostics for global health, *Annu. Rev. Biomed. Eng.* 1 (2008) 1–40, <https://doi-org.pbidi.unam.mx:2443/10.1146/annurev.bioeng.10.061807.160524>.
- [7] World Health Organization, Close to one billion people globally are served by health-care facilities with no electricity access or with unreliable electricity, Internet website, <https://www.who.int/news/item/14-01-2023-close-to-one-billion-people-globally-are-served-by-health-care-facilities-with-no-electricity-access-or-with-unreliable-electricity>.
- [8] A.K. Soe, S. Nahavandi, K. Khoshmanesh, Neuroscience goes on a chip, *Biosens. Bioelectron.* 35 (2012) 1–13, <https://doi-org.pbidi.unam.mx:2443/10.1016/j.bios.2012.02.012>.
- [9] P.A. Davidson, *An Introduction to Magnetohydrodynamics*, Cambridge Texts in Applied Mathematics, Cambridge University Press, 2001.
- [10] K.-M. Jan, S. Chien, Role of surface electric charge in red blood cell interactions, *J. Gen. Physiol.* 61 (1973) 638–654, <https://doi.org/10.1085/jgp.61.5.638>.
- [11] M.C. Weston, I. Fritsch, Manipulating fluid flow on a chip through controlled-current redox magnetohydrodynamics, *Sens. Actuators B, Chem.* 173 (2012) 935–944, <https://doi-org.pbidi.unam.mx:2443/10.1016/j.snb.2012.07.006>.
- [12] C. Murray, D. McCoul, E. Sollier, T. Ruggiero, X. Niu, Q. Pei, D. Di Carlo, Electro-adaptive microfluidics for active tuning of channel geometry using polymer actuators, *Microfluid. Nanofluid.* 14 (2013) 345–358, <https://doi-org.pbidi.unam.mx:2443/10.1007/s10404-012-1055-y>.
- [13] N.K. Ranjit, G.C. Shit, Joule heating effects on electromagnetohydrodynamic flow through a peristaltically induced micro-channel with different zeta potential and wall slip, *Physica A* 482 (2017) 458–476, <https://doi-org.pbidi.unam.mx:2443/10.1016/j.physa.2017.04.072>.
- [14] C. Qi, C. Wu, Electromagnetohydrodynamic flow in a rectangular microchannel, *Sens. Actuators B* 263 (2018) 643–660, <https://doi-org.pbidi.unam.mx:2443/10.1016/j.snb.2018.02.107>.
- [15] P. Woias, Micropumps-past, progress and future prospects, *Sens. Actuators B* 105 (2005) 28–38, <https://doi-org.pbidi.unam.mx:2443/10.1016/j.snb.2004.02.033>.
- [16] H.-J. Kang, B. Choi, Development of the MHD micropump with mixing function, *Sens. Actuators A* 165 (2011) 439–445, <https://doi-org.pbidi.unam.mx:2443/10.1016/j.sna.2010.11.011>.
- [17] S. Tenneti, S.G. Subramanian, M. Chakraborty, G. Soni, S. DasGupta, Magnetowetting of ferrofluidic thin liquid films, *Sci. Rep.* 7 (2017) 44738, <https://doi.org/10.1038/srep44738>.
- [18] G. Wu, M. Meyyappan, K.W.C. Lai, Simulation of graphene field-effect transistor biosensors for bacterial detection, *Sensors* 18 (2018) 5–14, <https://doi.org/10.3390/s18061715>.
- [19] M.I. Hasan, A.J.F. Ali, R.S. Tufah, Numerical study of the effect of channel geometry on the performance of Magnetohydrodynamic micro pump, *Int. J. Eng. Sci. Technol.* 20 (2017) 982–989, <https://doi-org.pbidi.unam.mx:2443/10.1016/j.jestch.2017.01.008>.
- [20] S. Parvin, N.C. Roy, L.K. Saha, Natural convective non-Newtonian nonfluid flow in a wavy-shaped enclosure with a heated elliptic obstacle, *Heliyon* 9 (2023) e16579, <https://doi-org.pbidi.unam.mx:2443/10.1016/j.heliyon.2023.e16579>.
- [21] A. Hussain, R. Zetoon, S. Ali, S. Nadeem, Magneto-hydro dynamic squeezed flow of Williamson fluid transiting a sensor surface, *Heliyon* 6 (2020) e04875, <https://doi-org.pbidi.unam.mx:2443/10.1016/j.heliyon.2020.e04875>.
- [22] C.G.N. Ketchate, P.T. Kapen, I. Madiebie-Lambou, D. Fokwa, V. Chegnimonhan, R. Tchinda, G. Tchien, Chemical reaction, Dufur and Soret effects on the stability of magnetohydrodynamic blood flow conveying magnetic nanoparticle in presence of thermal radiation: a biomedical application, *Heliyon* 9 (2023) e12962, <https://doi-org.pbidi.unam.mx:2443/10.1016/j.heliyon.2023.e12962>.
- [23] H.G. Weller, G. Tabor, H. Jasak, C. Fureby, A tensorial approach to computational continuum mechanics using object-oriented techniques, *Comput. Phys.* 12 (6) (1998) 620–631, <https://doi.org/10.1063/1.168744>.
- [24] A. Ebrahimi, E. Roohi, S. Kheradmand, Numerical study of liquid flow and heat transfer in rectangular microchannel with longitudinal vortex generators, *Appl. Therm. Eng.* 78 (2015) 576–583, <https://doi-org.pbidi.unam.mx:2443/10.1016/j.applthermaleng.2014.12.006>.
- [25] J.A. Sherclif, G.K. Batchelor, Steady motion of conducting fluids in pipes under transverse magnetic fields, *Proc. Camb. Philos. Soc.* 49 (01) (1952) 136–144, <https://doi.org/10.1017/S0305004100028139>.

- [26] A.P. Lee, J. Collins, A.V. Lemoff, A multi-functional micro total analysis system (μ TAS) platform for transport and sensing of biological fluids using microchannel parallel electrodes, in: M. Ferrari (Ed.), Volume IV: Biomolecular Sensing, Processing and Analysis, Springer, 2007, pp. 135–158, Ch. 7, ISBN: 978-0387-2556-8, <https://doi-org.pbidi.unam.mx:2443/10.1007/978-0-387-25845-4-7>.
- [27] J. Jang, S.S. Lee, Theoretical and experimental study of MHD (magnetohydrodynamic) micropump, *Sens. Actuators* 80 (2000) 84–89, [https://doi-org.pbidi.unam.mx:2443/10.1016/S0924-4247\(99\)00302-7](https://doi-org.pbidi.unam.mx:2443/10.1016/S0924-4247(99)00302-7).
- [28] J.-E. Ho, Characteristic study of MHD pump with channel in rectangular ducts, *J. Mar. Sci. Technol.* 15 (4) (2007) 315–321, <https://doi.org/10.51400/2709-6998.2048>.
- [29] M. Rivero, S. Cuevas, Theoretical analysis of the frictional losses in magnetohydrodynamic microflows considering slippage, *Microsyst. Technol.* (2019) 1–11, <https://doi-org.pbidi.unam.mx:2443/10.1007/s00542-019-04496-y>.
- [30] S. Lim, B. Choi, A study on the MHD (magnetohydrodynamic) micropump with side-walled electrodes, *J. Mech. Sci. Technol.* 23 (3) (2009) 739–749, <https://doi-org.pbidi.unam.mx:2443/10.1007/s12206-008-1107-0>.
- [31] S. Smolentsev, S. Cuevas, A. Beltrán, Induced electric current-based formulation in computations of low magnetic Reynolds number magnetohydrodynamic flows, *J. Comput. Phys.* 229 (2010) 1558–1572, <https://doi-org.pbidi.unam.mx:2443/10.1016/j.jcp.2009.10.044>.
- [32] Q. Li, M.-F. Yu, J. Li, X.-C. Zhang, H. Sun, Finite element analysis of effects of Joule heating, electro-osmosis and slip conditions on the performance of magnetohydrodynamic (MHD) micropumps, *Amer. Inst. Phys. Adv.* 8 (2018) 075330, <https://doi.org/10.1063/1.5029849>.
- [33] Y. Chen, C.N. Kim, Numerical analysis of the mixing of two electrolyte solutions in an electromagnetic rectangular micromixer, *J. Ind. Eng. Chem.* 60 (2018) 377–389, <https://doi-org.pbidi.unam.mx:2443/10.1016/j.jiec.2017.11.025>.
- [34] A. Alipour, M.H. Korayem, D. Younesian, Design and simulation of a magnetohydrodynamic micro-pump to provide time varying tensile force for vibration suppression in viscoelastic micro-beams, *J. Mech. Sci. Technol.* 33 (5) (2019) 2149–2159, <https://doi-org.pbidi.unam.mx:2443/10.1007/s12206-019-0417-8>.
- [35] S. Derakhshan, K. Yazdani, 3D analysis of magnetohydrodynamic (MHD) micropump performance using numerical method, *J. Mech.* 32 (01) (2016) 55–62, <https://doi.org/10.1017/jmech.2015.39>.
- [36] J. Martinez, E. Polatdemir, Origin of the Hartman effect, *Phys. Lett. A* 351 (1) (2006) 31–36, <https://doi-org.pbidi.unam.mx:2443/10.1016/j.physleta.2005.10.076>.
- [37] S. Qian, H.H. Bau, Magneto-hydrodynamics based microfluidics, *Mech. Res. Commun.* 36 (1) (2009) 10–21, <https://doi.org/10.1016/j.mechrescom.2008.06.013>.
- [38] M.A. Ramírez-Trocherie, *Generadores Magneto-Hidrodinámicos*, Master's thesis, Universidad Nacional Autónoma de México, Fac. de Ing., 2019.
- [39] T.L. Sounart, T.A. Michalske, K.R. Zavadil, Frequency-dependent electrostatic actuation in microfluidic MEMS, *J. Microelectromech. Syst.* 14 (2022) 125–133, <https://doi.org/10.1109/JMEMS.2004.839006>.
- [40] G. Ibañez, S. Cuevas, M. López de Haro, Optimization analysis of an alternate magnetohydrodynamic generator, *Energy Convers. Manag.* 43 (2002) 1757–1771, [https://doi.org/10.1016/S0196-8904\(01\)00133-9](https://doi.org/10.1016/S0196-8904(01)00133-9).
- [41] G.B. Arfken, H.J. Weber, *Mathematical Methods for Physicists*, Academic Press, 1995.
- [42] M. Rivero, S. Cuevas, Analysis of the slip condition in magnetohydrodynamic (MHD) micropumps, *Sens. Actuators B* 166–167 (2012) 884–892, <https://doi-org.pbidi.unam.mx:2443/10.1016/j.snb.2012.02.050>.
- [43] H. Jasak, *Error analysis and estimation for the finite volume method with applications to fluid flows*, Ph.D. thesis, Imperial College of Science, Technology and Medicine, 1996.
- [44] R. Issa, Solution of the implicitly discretised fluid flow equations by operator-splitting, *J. Comput. Phys.* 61 (1985) 39–65, [https://doi-org.pbidi.unam.mx:2443/10.1016/0021-9991\(86\)90099-9](https://doi-org.pbidi.unam.mx:2443/10.1016/0021-9991(86)90099-9).
- [45] E.M. de, les Valls, Development of a simulation tool for mhd flows under nuclear fusion conditions, PhD thesis, Universitat Politècnica de Catalunya, October 2011, available at <http://www-fusion.ciemat.es/PhDThesis/MasdelesValls.pdf>, 2011.
- [46] I.E. Barton, Comparison of the simple- and piso-type algorithms for transient flows, *Int. J. Numer. Methods Fluids* 26 (1998) 459–483.
- [47] Openfoam foundation, mhdFoam.C solver, Internet website, https://www.openfoam.com/documentation/guides/latest/api/mhdFoam_8C_source.html.
- [48] Openfoam foundation, Openfoam v6, Internet website. URL, <https://openfoam.org/download/>.
- [49] K. Ito, T. Takahashi, T. Fujino, M. Ishikawa, Influences of channel size and operating conditions on fluid behavior in a MHD micro pump for micro total analysis system, *J. Int. Council Electr. Eng.* 4 (3) (2014) 220–226, <https://doi.org/10.5370/JICEE.2014.4.3.220>.
- [50] J.P. Holman, *Experimental Methods for Engineers*, McGraw-Hill International Edition, 2011.
- [51] J.J. Sniegowski, E.J. Garcia, Microfabricated actuators and their application to optics, in: *Micro-Optics/Micromechanics and Laser Scanning and Shaping*, in: *Proc. SPIE*, vol. 2383, 1995, pp. 46–64.